Driving of outer belt electron loss by solar wind dynamic pressure structures: Analysis of balloon and satellite data

A. W. Breneman[1], A. J. Halford[2], R. M. Millan[3], L. A. Woodger[3], X-J. Zhang[4], J. K. Sandhu[5], L. Capannolo[6], W. Li[6], Q. Ma[6], C. M. Cully[7], K. R. Murphy[2], T. Brito[8] , S. S. Elliott[9]

[1] School of Physics and Astronomy, University of Minnesota, Twin Cities, Minneapolis, MN, USA.

[2] NASA Goddard Space Flight Centre, Greenbelt, MD, USA.

[3] Department of Physics and Astronomy, Dartmouth College, Hanover, New Hampshire, USA.

[4] Institute of Geophysics and Planetary Physics, University of California, Los Angeles, CA, USA.

[5] Northumbria University, Newcastle upon Tyne, UK

[6] Center for Space Physics, Boston University, Boston, MA, USA.

[7] Department of Physics and Astronomy, University of Calgary, Calgary, AB, Canada.

[8] Department of Physics, University of Helsinki, Helsinki, Finland.

[9] Department of Physics and Astronomy, University of Iowa, Iowa City, IA, USA.

Corresponding author: Aaron W. Breneman (awbrenem@gmail.com)

Key Points:

- We report on large-scale driving of electron precipitation from outer belt by commonly-observed ~1 hr duration solar wind pressure structures
- The resulting forced breathing of magnetosphere causes ExB drift which modulates population of 10s keV electrons
- These electrons trigger growth of hiss waves which, in turn, modulate precipitation loss observed as X-rays on BARREL

Abstract

We present observations of ~10-60 min solar wind dynamic pressure structures that drive large-scale coherent ~20-100 keV electron loss from the outer radiation belt. A combination of simultaneous satellite and Balloon Array for Radiation-belt Relativistic Electron Losses (BARREL) observations on Jan 11-12, 2014 show a close association between the pressure structures and precipitation as inferred from BARREL X-rays. Specifically, the structures drive radial ExB transport of electrons up to 1 Earth radii, modulating the free electron energy available for low frequency plasmaspheric hiss growth, and subsequent hiss-induced loss cone scattering. The dynamic pressure structures, originating near the Sun and commonly observed advecting with the solar wind, are thus able to switch on scattering loss of electrons by hiss over a large spatial scale. Our results provide a direct link between solar wind pressure fluctuations and modulation of electron loss from the outer radiation belt and may explain long-period modulations and large-scale coherence of X-rays commonly observed in the BARREL dataset.

Plain Language Summary

The Earth's low-density magnetosphere is a region of enclosed magnetic field lines that contains energetic electrons ranging from eV to MeV energies. These populations can be greatly enhanced in response to solar driving. Following enhancements, energetic electron populations are depleted on timescales of hours to days by various processes. One important depletion process occurs when an electromagnetic plasma wave called plasmaspheric hiss, which exists within a high plasma density region called the plasmasphere and its (occasional) radial extension called the plume, scatters energetic electrons into the atmosphere. In this paper, we show that these hiss waves can be switched on by compressions of the magnetosphere which occur in response to ~1 hr long pressure structures in the solar wind. These structures originate at or near the Sun and are very common in the solar wind at 1 AU. The newly-excited hiss waves scatter electrons into the atmosphere where they are observed on balloon-borne X-ray detectors. Our results suggest that magnetospheric models that predict the loss of electrons from hiss waves may be improved by consideration of solar wind pressure-driven dynamics.

1 Introduction

Ultra-low frequency (ULF) waves, ranging from seconds to minutes, are a frequent feature of the Earth's magnetosphere and are important drivers of magnetospheric dynamics (Elkington and Sarris, 2016). They can enhance particle transport (Ukhorskiy et al., 2006), accelerate particles via drift resonance (Elkington et al., 2003), and modify loss rates of electrons due to both magnetopause shadowing (Turner et al., 2012; Mann et al., 2016) and scattering loss into the atmosphere (Brito et al., 2020). ULF waves, with sources both internal and external to the magnetosphere (Zhu and Kivelson, 1991), can couple into various magnetospheric modes

such as field line resonances (e.g. Dungey 1954 a,b; Southwood, 1974) and fast mode cavity resonances (Hartinger et al., 2013).

Longer period variations - more than about 16 minutes - of magnetospheric fields and plasma are also observed, typically in association with external drivers including solar wind dynamic pressure structures (Agapitov and Cheremnykh, 2013; Kepko and Spence, 2003). These *mesoscale* structures, near-ubiquitous features advecting with the solar wind (Viall et al., 2009; Kepko et al., 2020), likely originate at or near the sun, possibly in association with the formation of the slow solar wind (Viall and Vourlidas, 2015; Kepko et al., 2016). They tend to be grouped into discrete scale sizes, with observed frequency a function of this size and the solar wind speed (Kepko and Spence, 2003; Viall et al., 2008). Because of their slow variation and large scale size they do not couple into the magnetosphere as modes, field-line resonances, or propagating waves, but instead drive a quasi-static magnetospheric response as the balance between internal magnetic and external dynamic pressure (e.g. Kepko et al., 2002; Kepko and Viall, 2019; Glassmeir et al., 2008). This response, sometimes described as a *forced-breathing*, can be observed on satellites as oscillations of magnetic field, density, energetic particle flux, and wave amplitudes (e.g. Xia et al., 2016). Similar periodicities are also commonly observed in signatures of precipitating electron flux from balloons (Foat et al., 1998; Millan et al., 2011), and ground based observatories over a wide range of latitudes including riometers (Spanswick et al., 2005), magnetometers (Villiante et al., 2007; Villiante et al., 2016; Kepko and Spence, 2003), and high frequency radars that measure ionospheric plasma flow variations (Fenrich and Waters, 2008; Stephenson and Walker, 2002; Dyrud et al., 2008). Taken together, these suggest an important role for periodic solar wind structures in driving magnetospheric dynamics and magnetosphere-ionosphere coupling (Shi et al., 2020).

Because of a historical lack of simultaneous measurements in the solar wind, magnetosphere, and atmosphere, it has been difficult to experimentally establish a relationship between external driving on ULF and forced-breathing timescales and electron loss. Breneman et al., 2015 showed that 1-10 min ULF modulations of X-ray flux on a BARREL balloon (Millan et al., 2013; Woodger et al., 2015) were nearly identical to modulations in whistler-mode plasmaspheric hiss amplitude observed on the Van Allen Probes (Mauk et al., 2012) during a close magnetic conjunction. Similar modulations of magnetic field and plasma density were observed throughout much of the magnetosphere, establishing the existence of a new global coherence scale of electron loss. However, that study was unable to identify the source of the driving.

In this paper we discuss an event on Jan 11-12, 2014 where global-scale modulations of magnetospheric plasma and magnetic field have an identified cause; long period (tens to ~60 min) solar wind dynamic pressure structures that drive a forced-breathing of the magnetosphere. This forcing acts as a switch turning on low frequency plasmaspheric hiss that scatters electrons into the atmosphere where they are observed as X-rays on the balloons. This type of driving can explain commonly observed modulations in BARREL X-rays, and these results have implications for predictions of electron loss on timescales of hours to days.

2 Observations

2.1 Conjunction observations (overview)

Figure 1 shows an overview of balloon and satellite observations on Jan 11-12, 2014 when solar wind pressure structures strongly modulate electron loss from the outer radiation belt. From ~22-23 UT on Jan 11, THEMIS-A and BARREL 2X have a close magnetic conjunction, as shown in the dial plot. During this conjunction it is likely that THEMIS-A is in a plasmaspheric plume. At ~19:18 UT a substorm (panel a) resulted in the injection of 10-100s keV energetic electrons into the outer belt. An increase in energetic electrons around this time is observed on THEMIS-A (panel b), but this may be due to its outbound entry into the outer belt at L~4. Following substorm onset the solar wind dynamic pressure (panel c, OMNI database time-shifted from Wind data 195 Earth radii (RE) upstream) generally increased and included significant fluctuations on ~10-60 min scales. The magnetosphere, in general, responds to slow pressure driving by varying its size until a balance between internal magnetic pressure and external solar wind dynamic pressure is achieved. THEMIS-A enters a plume near 21:40 UT (density in panel d from the Electrostatic Analyzer instrument (ESA, McFadden et al., 2009)) and these dynamic pressure fluctuations are thereafter observed to modify energetic electron flux (panel b), wave amplitude at frequencies consistent with the whistler mode (panel e), and precipitating electron flux (via X-rays on BARREL 2X, panel f).

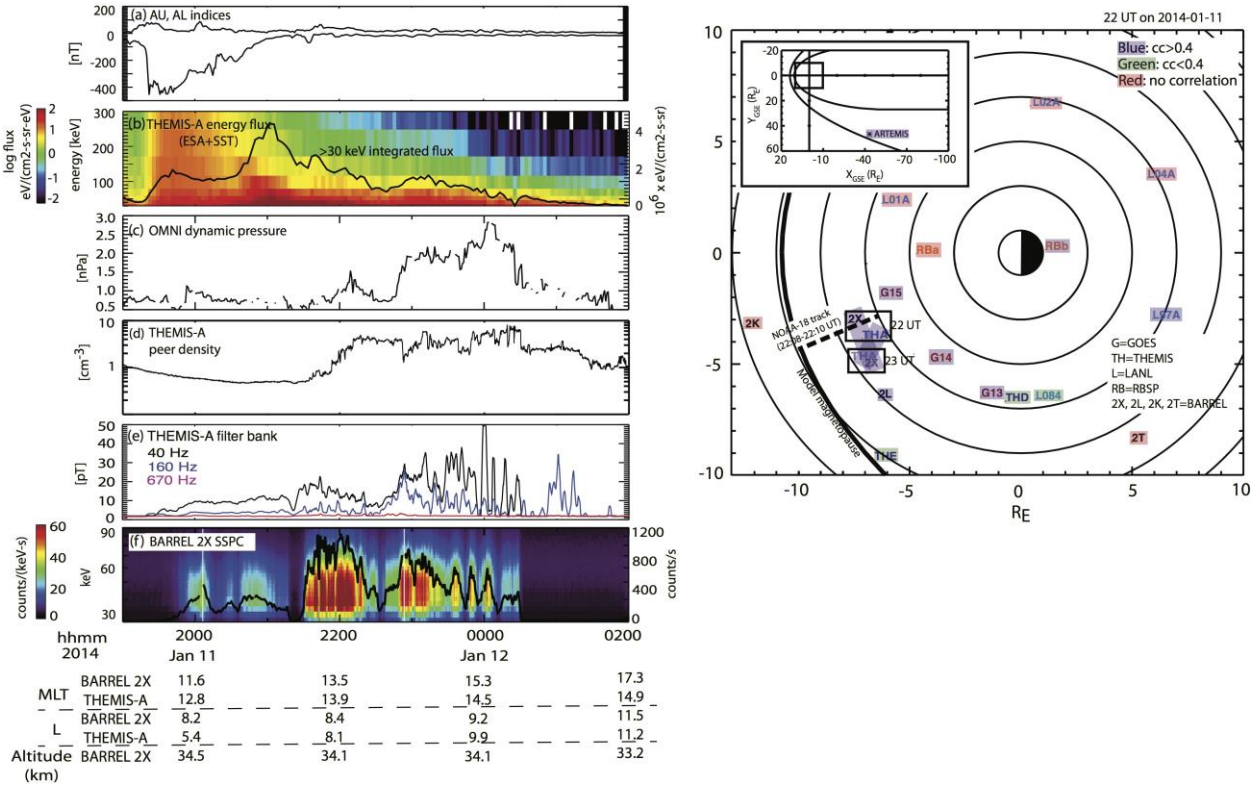

Figure 1: Left column is an overview of the solar wind pressure fluctuation driven event on Jan 11-12, 2014. (a) AU, AL indices showing a substorm onset at ~19:18 UT that injects 10s keV electrons into the outer belt. (b) An increase in electron flux is observed on THEMIS-A near this time, but this may be due to it entering into the outer belt on its outbound orbit. The integrated >30 keV electron flux is shown as the line with scale on the right. (c) Solar wind dynamic pressure (OMNI database) showing significant variation over minutes to hours. (d) Near the time

THEMIS-A enters a plume - observed as a density increase at 21:40 UT on the ESA instrument - these variations cause similar modulations in (e) low frequency ~40 Hz wave amplitude, and (f) precipitating electron flux, observed as X-rays in the BARREL 2X slow spectral product (SSPC, with the black line showing the integrated SSPC X-ray flux for >30 keV). Right plot: Equatorially mapped (T89 model with Kp=2) L, MLT location of various payloads at 22 UT on Jan 11th. The boxed regions show THEMIS-A and BARREL 2X at 22 and 23 UT, and the nearby dashed line shows the NOAA-18 track at 22 UT, highlighting what we define as the conjunction studied in this paper. Payload shades indicate the maximum value of the cross-correlation calculated by time shifting relevant quantities on each payload (e.g. plasma, magnetic field, or precipitation-related) with the solar wind pressure fluctuations. The influence of the solar wind driving is clearly seen on payloads with coefficients >0.4 (purple-shaded), less clearly on payloads with coefficients <0.4 (green-shaded), and not at all for red-shaded payloads. The inset shows the downstream flank location of the ARTEMIS satellites, which clearly observe the solar wind pressure fluctuations. The magnetopause model is from Roelof and Sibeck, 1993.

Similar sorts of fluctuations are also observed on BARREL 2L and on other satellites spanning a wide range of L and post-noon MLT including the low-density magnetosphere, plasmasphere, and on ARTEMIS at ~40 RE downstream in the magnetosheath. Relative timing of these fluctuations on near-geosynchronous payloads and with ARTEMIS indicates an overall duskward propagation of ~300 km/s, similar to the solar wind flow velocity of ~400 km/s. Taken together, these observations are consistent with global-scale change in the magnetosphere cavity size externally driven by the large-scale dynamic pressure structures.

Panels e and f in Figure 1 show that wave amplitudes near 40 Hz (THEMIS-A filter bank instrument, Cully et al., 2008) and X-rays on BARREL 2X abruptly increase at 21:25 UT and 21:30 UT, respectively. The dynamic pressure does increase around this time, but only by a small amount. The 2X increase may be primarily a spatial effect related to its field of view (a circle of ~1 RE diameter at the magnetic equator) magnetically mapping into a plume. Plume entry for THEMIS-A likely occurs near 21:40 UT, as suggested by a small density increase shown in Figure 1, panel d. The ~40 Hz wave amplitude increase from 21:25 to 21:40 UT may be the result of pressure-modulated chorus or exohiss (Zhu et al., 2015) wave populations near the plume boundary.

Further evidence for the existence of a plume in this region comes from an enhanced density region observed on prior and subsequent crossings of various satellites (including the Van Allen Probes) within a few hours of the conjunction. In addition, a cross-phase analysis (e.g. Waters et al., 1991; Menk et al., 2014) of CARISMA ground magnetometer stations (Mann et al., 2008) from L=4-7 at similar MLT shows no evidence of a sharp gradient in plasma density as a function of radial distance, indicating an extended plasmasphere. We thus conclude that the conjunction occurs within a plume. This suggests that the ~40 Hz waves after 21:40 UT from Figure 1e are most likely low frequency plasmaspheric hiss. This identification is further discussed in Section 2.3.

These observations indicate that variations in solar wind pressure on timescales of ~10-60 min can cause similar variations in electron precipitation from the outer belt. We now focus on detailed observations to understand how this occurs.

2.2 Conjunction observations (detailed)

Figure 2 plots relevant quantities near the 22-23 UT conjunction from OMNI, BARREL 2X, THEMIS-A, and RBSP-A, detrended to clearly show the direct manner in which the solar wind pressure fluctuations modulate various plasma quantities and, ultimately, electron precipitation. Comparison of similar modulations observed in the magnetic field on THEMIS-A and dynamic pressure from OMNI indicate that the uncertainty in the OMNI data timing is likely no more than ~10 min throughout this period. This chain of events is summarized as follows: the dynamic solar wind pressure enhancements compress the magnetosphere, as observed by increases in the compressional magnetic field (panel a). This results in a global-scale ExB non-dispersive radial transport (panels b and c), observed as fluctuations in >30 keV electron flux on THEMIS-A (panel d). These fluctuations in electron free energy modulate wave amplitude near 40 Hz (panel e) which modulates X-rays caused by precipitating electrons (panel f).

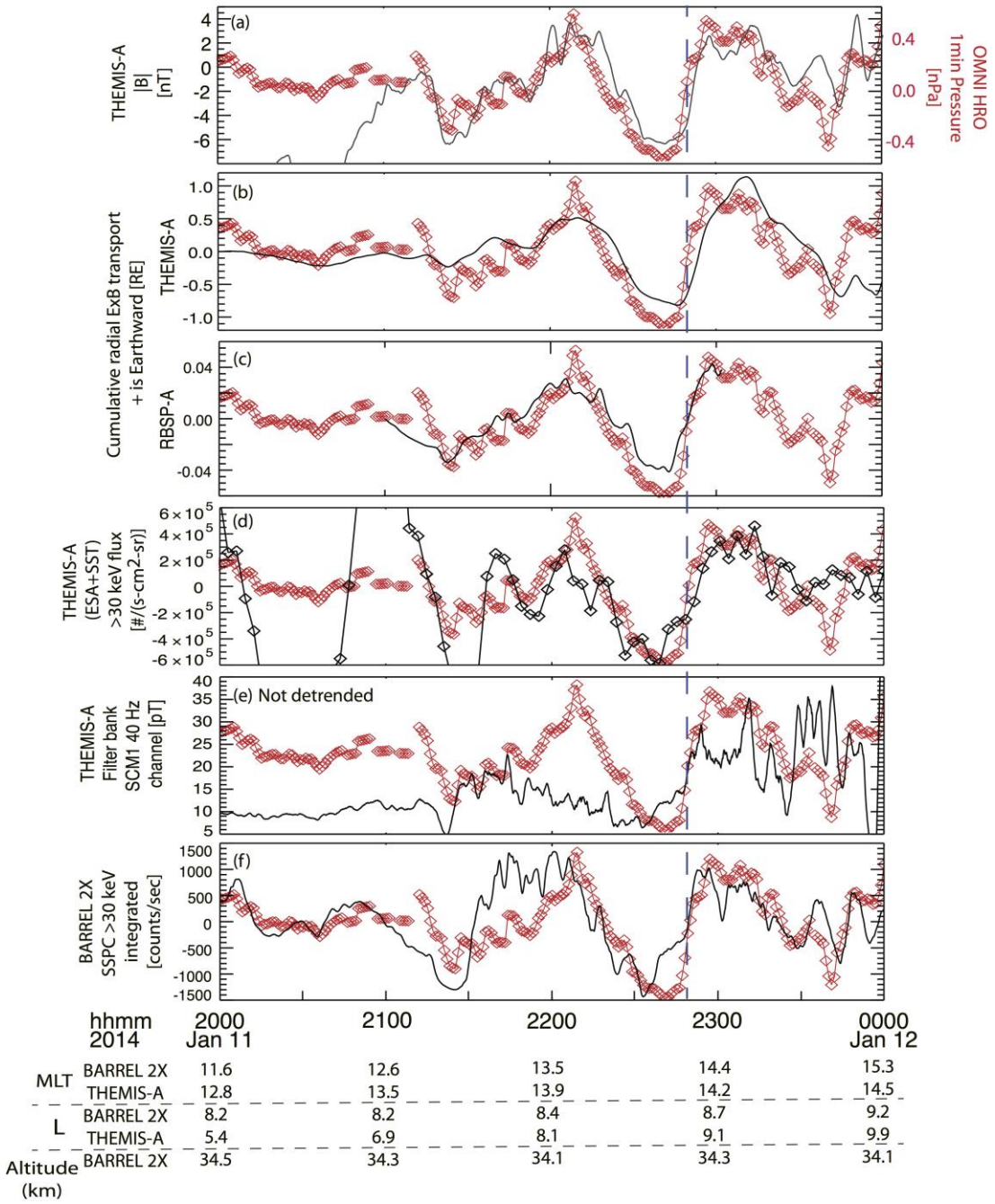

Figure 2: Relevant THEMIS-A and BARREL 2X quantities smoothed over 2 min and detrended over 80 min using a boxcar technique to show the influence of OMNI solar wind pressure variations (red curve in each panel) on (a) the magnetospheric magnetic field; (b, c) the radial ExB transport of plasma as observed by THEMIS-A and RBSP-A, respectively; (d) the integrated >30 keV electron flux; (e) the growth of ~40 Hz waves (not detrended). These (likely) hiss waves ultimately cause (f) variations in the X-ray precipitation signatures as observed in the BARREL 2X slow spectral data (SSPC) for >30 keV energies. The detrending has been tested to be robust to different techniques and for periods >60 min.

A more detailed explanation of this chain of events starts with the understanding that the observed tens of minutes to ~1 hr solar wind pressure fluctuations are much longer than the

response time of the magnetosphere to such driving. Namely, the magnetosphere communicates cavity size changes on the order of the fast mode travel time from subsolar point to the inner magnetosphere, typically less than 16 min (<3 mHz). The magnetosphere responds quasi-statically to changes in external driving that occur more slowly than this. The observed tens of minutes to ~1 hr magnetic field fluctuations are thus not ULF waves or cavity modes, but are rather semi-periodic modulations of the overall magnetosphere cavity size (forced breathing). In response to this breathing, electrons ExB drift, primarily radially for this event. Figure 2b shows the estimated cumulative effect of this radial drift calculated from observed electric and magnetic fields on THEMIS-A from 20-24 UT when it was outbound at MLTs from 12.8 to 14.5 and L values from 5.4 to 10. Electrons at <200 keV have drift periods longer than the ~1 hr driving period and would be radially transported up to 1 RE in response to the forced breathing. A similar calculation for RBSP-A from 21-24 UT, at MLTs from 10.6 to 13.7 and L values from 3.3 to 5.9, indicates that this driven transport (though small at this location) can be observed across a large range of MLTs and to low L values, and is thus nearly global in nature. Electrons with higher energies have drift periods shorter than 1 hr and would drift out of the modulated dayside region before experiencing the full effect of the driving. As these tens keV electrons near the location of THEMIS-A drift inwards by 1 RE to a stronger magnetic field region over 30 min (half the 1 hr driving period) they will gain a few keV of energy from conservation of the first adiabatic invariant (e.g. Roederer and Zhang 2014 Eqn. 3.37).

In addition, applying the calculated ExB drift (Figure 2b) to the observed >30 keV radial flux gradient from NOAA-18 Polar Orbiting Environmental Satellite (POES, Evans and Greer, 2004; see track in Figure 1) predicts similar flux variation to the actual >30 keV flux variation observed on THEMIS-A (Figure 2d). Comparison of additional dayside POES satellite passes in the post noon sector near this time span suggests that this radial gradient is relatively static. NOAA-18 observations are discussed in more detail in Section 3.

All the available observations show that the fluctuations of 10s keV electrons from ~20-24 UT on Jan 11 is consistent with ExB non-dispersive radial transport driven by the solar wind pressure fluctuations. With the connection between the external driving and the magnetospheric response established, we now examine the resulting increase in ~40 Hz wave power and its role in the electron precipitation.

2.3 Hiss wave observations

Figure 1e plots THEMIS-A filter bank wave magnetic field power near 40 Hz, showing a close correspondence with the solar wind pressure. Unfortunately, no spectral, burst waveform, or polarization data are available during the conjunction for precise determination of wave frequency and properties. However, the filter bank, which records the peak wave magnetic and electric field amplitudes every 4 sec, has sufficient frequency resolution (6 bins with peak responses at 2.5, 9, 40, 160, 670, and 2500 Hz) that we can show that this power likely corresponds to low-frequency plasmaspheric hiss (Li et al., 2013; 2015; 2019; Ni et al., 2014; Malaspina et al., 2017).

Wave power during the conjunction generally peaks in the 40 Hz bin but is also observed in the 160 Hz and 670 Hz bins, indicating that the frequency of peak power is close to but above 40 Hz. This is similar to the local lower hybrid frequency of f_{lh}~40 to 50 Hz from 21:30 to 24 UT. Magnetosonic whistler mode waves (Boardsen et al., 2016) are not common at frequencies

252 $f>f_{lh}$ (Ma et al., 2013) and are thus likely ruled out. At lower frequencies, a lack of wave power
253 in the 2.5 Hz and 9 Hz bins rules out broadband temporal structures (e.g. Mozer et al., 2015) and
254 low frequency electromagnetic ion cyclotron (EMIC) waves. Kinetic Alfven Waves are ruled out
255 because the observed ratio of wave magnetic to electric fields (not shown) is too high, and
256 because they are not common near noon MLT (Chaston et al., 2013). Prior to 21:40 UT, when
257 THEMIS-A is likely outside of the plume the waves may be low frequency chorus (Cattell et al.,
258 2015) or exohiss (e.g. Zhu et al., 2015). After the plume entry at 21:40 UT the available evidence
259 suggests that the >40 Hz wave power is low frequency whistler-mode hiss. Further support for
260 this identification comes from the observation that the wave power is continuous over a broad
261 region, and that low frequency hiss waves would be unstable to the 10s keV electrons drifting
262 into the plume following the ~19:18 UT substorm. Finally, hiss waves can plausibly produce the
263 precipitation observed as 10s keV X-rays on BARREL. This is not true of EMIC waves which
264 scatter higher energy electrons (e.g. Chen et al., 2016), or magnetosonic waves which only affect
265 electrons at large pitch angles (Ma et al., 2016; Fu et al., 2019). Therefore, despite having limited
266 wave data available we are able to identify these waves as low frequency plasmaspheric hiss. It
267 is these waves that are subsequently modulated in sync with the ExB transport motion driven by
268 the solar wind dynamic pressure fluctuations.

269

270

271 **3 Satellite and balloon spectral and flux comparison**

272

273 We conclude discussion of the aforementioned chain of events with a close comparison
274 of satellite and balloon observations to establish that the observed X-rays on BARREL 2X
275 correspond to electron loss to the atmosphere caused by low frequency plasmaspheric hiss
276 scattering. Evidence for this connection includes spectral similarities between near loss cone
277 electrons on THEMIS-A and X-rays on BARREL 2X, and consistency between predicted loss
278 rates from THEMIS-A and the observed loss rates on NOAA-18.

279 We start by establishing the energy range of precipitated electrons. Figure 3a shows the
280 THEMIS-A number flux spectra during the local peak in flux from 21:45-22:05 UT for the field-
281 aligned pitch angle bin (0-22.5^{o}). Flux peaks in energy from 20-30 keV and falls by a factor of
282 ~50 by 100 keV. Some unmeasured fraction of these electrons are at or near the loss cone and
283 can be precipitated within a bounce-period by the observed hiss. NOAA-18 low altitude
284 observations (proton contamination removed, Figures 3b, c) with both the 0^{o} and 90^{o} telescopes,
285 proxies for precipitating and trapped fluxes, respectively, offer a low earth orbit perspective on
286 precipitating electrons. At ~800 km altitude the 0^{o} telescope looks deep within the loss cone and
287 thus measures a lower limit to the precipitating flux. Figure 3b shows that the >30 keV flux is
288 significantly higher than the >100 keV flux in the 0^{o} telescope during the MLT~13 pass from
289 L=8-11 (22:08 to 22:09:30 UT). In addition, panel c shows that the flux ratio (0^{o}/90^{o}) is close to
290 unity at L>8 for >30 keV channel but is much smaller for the >100 keV channel. These two
291 observations indicate strong loss cone scattering for energies <100 keV and are consistent with
292 the THEMIS-A electron observations. These ~30 to <100 keV scattered electrons then

precipitate into the atmosphere where they can create the 30 to <100 keV Bremsstrahlung X-rays that are detected by BARREL 2X, as shown in Figures 1 and 2.

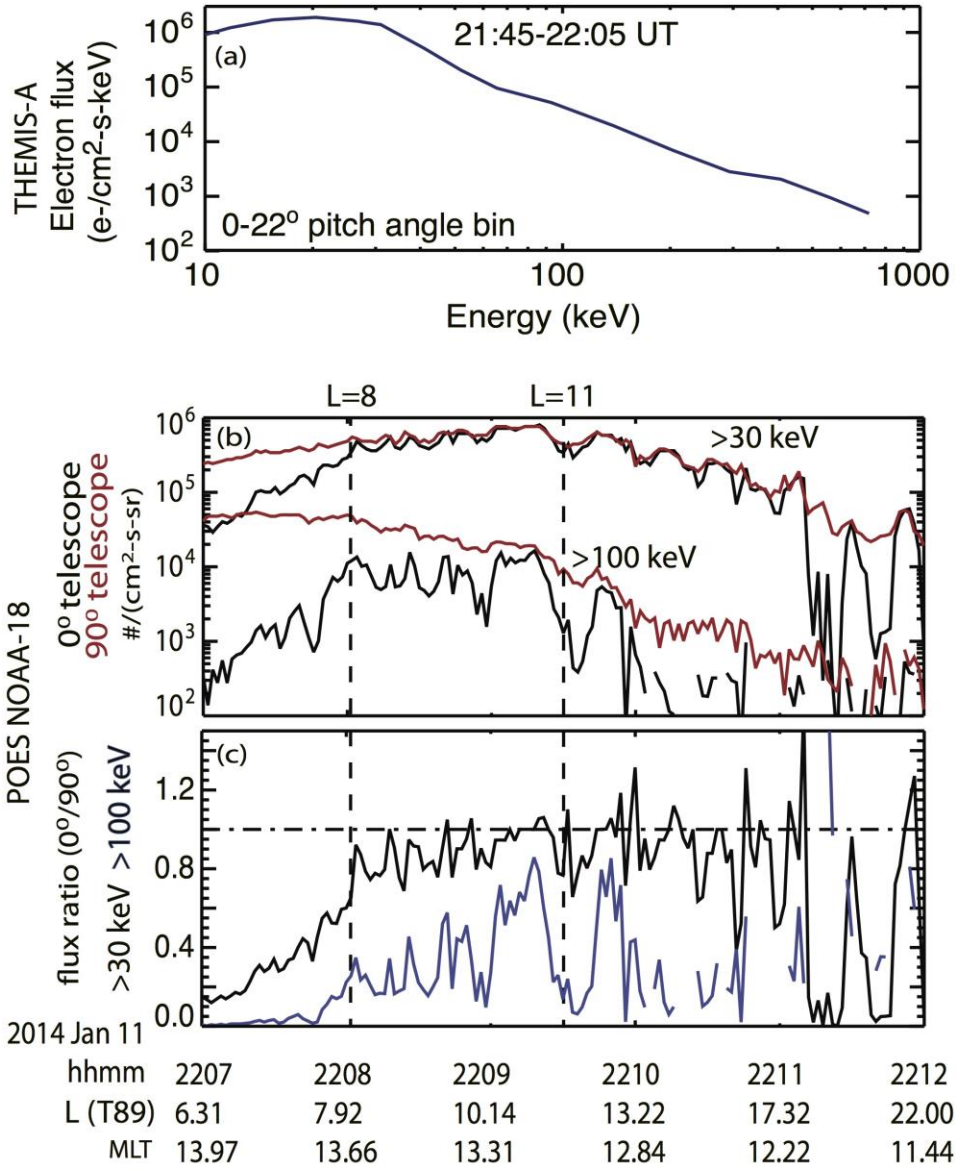

Figure 3: Comparison of THEMIS-A observations to NOAA-18 SEM-2 (Space Environment Monitor 2) observations from an MLT=13 pass through the outer belt (see Figure 1). (a) THEMIS-A field-aligned electron flux vs energy showing a large fall off by 100 keV. (b) NOAA-18 electron number flux observations in the 0° (black) and 90° (red) telescopes for the >30 keV and >100 keV energy channels. The near overlap of the black and red for the >30 keV channel at L>8 indicates scattering near the strong diffusion limit. (b) NOAA-18 flux ratio (0°/90°) for both channels indicates that the scattering efficiency falls off significantly by 100 keV energies. The vertical lines indicate when NOAA-18 is in the region of interest from L=8-11. NOAA-18 proton contamination has been removed with the method described in Peck et al., 2015.

We now compare >30 keV loss rates on THEMIS-A and NOAA-18. These should be similar if the precipitating electrons observed on NOAA-18 come from the same large-scale

modulated source region observed on THEMIS-A. From Figure 3b, the >30 keV loss cone number flux from the NOAA-18 0° telescope from L=8 to L=11 ranges from $5x10^5$-$8x10^5$ $(cm^2\text{-}s\text{-}sr)^{-1}$. Because number flux is invariant along a magnetic field line we can directly compare this range to THEMIS-A ESA estimated loss cone flux during the conjunction. Integrating the lowest pitch angle bin (0-22.5°) flux for >30 keV energies at 22:05 UT (L~8) gives $2x10^6$ $(cm^2\text{-}s\text{-}sr)^{-1}$. This is larger than the NOAA-18 flux by a factor of ~2.5-5. However, due to the large bin size, THEMIS-A would be overestimating the loss cone flux for an anisotropic pitch angle distribution (more electrons near 22.5° than the loss cone), and NOAA-18 may be an underestimating the flux if there are more electrons at the edge of the loss cone than deep within it. Other sources of error include less than perfect subtraction of NOAA-18 proton contamination, unaccounted for spatial or temporal structure in the hiss source region, and off-equatorial (above the 5° magnetic latitude of THEMIS-A) hiss-caused electron scattering. Considering the difficulty of comparing low and high-altitude observations, the NOAA-18 and THEMIS-A fluxes can be considered in rough agreement, indicating that the two are observing a different aspect of hiss-induced loss cone scattering from the same large-scale modulated precipitation region.

4 Relation of observed electron loss to hiss

We now compare the predicted rate of electron scattering into the loss cone from the observed hiss waves to the actual loss rate to determine if the hiss waves are indeed capable of providing the modulated electron loss. The flux ratio (0°/90°) of NOAA-18 >30 keV electrons in Figure 3c is close to but less than unity at L=8 but approaches unity from L=10-12, indicating particularly strong scattering. This overall strong precipitation region is persistent and is observed on multiple POES satellites during ~20:00-24:00 UT from 10-15 MLT in the outer belt. The observed hiss waves must be capable of providing this strong scattering over this region. The same is not true for >100 keV energies (Figure 3b) which show significantly weaker scattering.

It is well established that scattering caused by small amplitude waves can be accurately described as quasi-linear diffusion (Bortnik et al., 2016). Figure 4 presents our determination of the diffusive bounce-averaged scattering rate near the loss cone ($\langle Daa \rangle_{LC}$) from two model runs representing times of peak magnetospheric compression near 22 and 23 UT. Input parameters include the average hiss amplitude and frequency distribution, as well as plasma density and magnetic field determined from five-minute averages of THEMIS-A data (panels a, b). The magnetic field and wave amplitude are well-determined quantities, while the wave frequency distribution and plasma density can only be roughly estimated from the limited data. We have chosen 40 Hz as the peak frequency based on discussion in Section 2.3. Model results are provided for two density values: 5 cm^{-3} for both runs represents the likely lower density limit (obtained from THEMIS-A ESA data), and upper limits of 53 cm^{-3} for 22 UT and 21 cm^{-3} for 23 UT (obtained with THEMIS-A Electric Field Instrument (EFI) antenna potentials, Bonnell et al., 2009). The correct density values likely lie between these extremes.

The model $\langle Daa \rangle_{LC}$, proportional to the square of the wave magnetic amplitude, is plotted for both runs as a function of energy in Figure 4c, d. For the first run (~22 UT, corresponding to THEMIS-A at L~8) the diffusion rate for 10s keV electrons does not reach the strong diffusion limit due to insufficient average hiss amplitude. The rate is, however, still large

enough to drive the significant loss observed by NOAA-18 in Figure 3b at L=8. For the second run (~23 UT corresponding to THEMIS-A at L~10) the average hiss amplitude is larger, and the strong diffusion limit is reached for <100 keV energies for the entire range of possible densities, consistent with the NOAA-18 observations in Figure 3b at L=10-11. The range of possible peak scattered energies for both runs (~10-100 keV) is also consistent with the range of electron energies observed on THEMIS-A (Figures 1b; 3a) and X-rays on BARREL 2X (Figure 1f).

These modeling results strongly suggest that the observed modulated hiss waves are causing the scattering that is observed on 2X. The observation that the precipitating flux is greater near 22 UT than 23 UT, despite the hiss amplitudes being larger near 23 UT, may be explained by the increased availability of >30 keV flux near 22 UT, as seen in Figure 1b. This is discussed further in Section 5.

We briefly note that it has been suggested (e.g. Halford et al., 2015; Brito et al., 2020) that electron loss can be driven directly by ULF fluctuations via loss cone modulation, without the intermediary of higher frequency wave scattering. This modulation affects inward drifting electrons as the loss cone angle increase outpaces the electrons' pitch angle increase from first (and competition from second) adiabatic invariant conservation. This can also occur for local electrons by direct loss cone size modulation from compressional ULF waves (Rae et al., 2018). Due to the long forced breathing period (~1 hr) and the inward ExB drift of only about 1 RE the estimated loss rates due to these effects are orders of magnitude lower than observed during the Jan 11 conjunction.

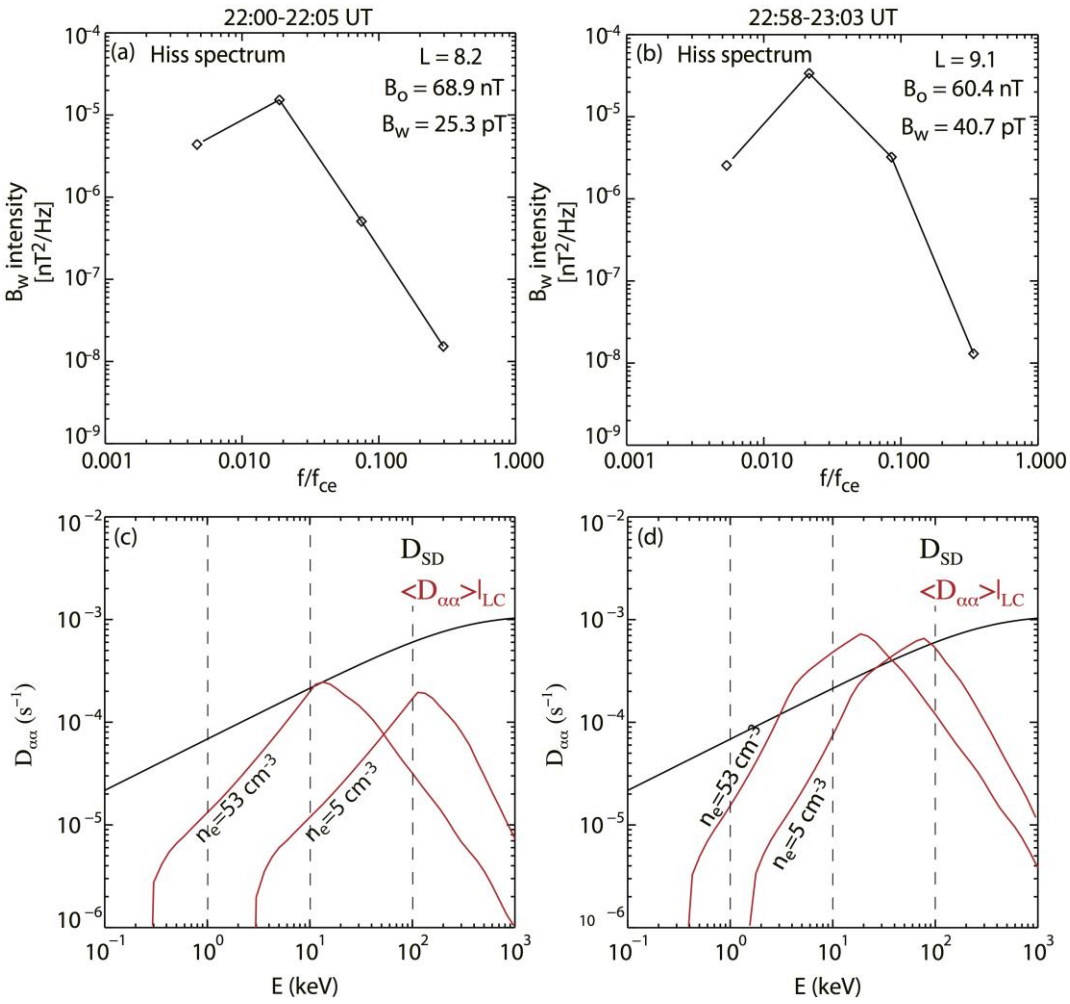

Figure 4: Bounce-averaged pitch angle diffusion rate (<Daa>) results for two model runs, at 22 and 23 UT (left and right columns, respectively). (a, b) the hiss spectra as well as best-determined input parameters from THEMIS-A for each model run. The wave intensity is listed as 2 times the observed value to account for the fact that the filter bank only measures a single wave component. (c, d) model <Daa> evaluated at the loss cone (<Daa>$|_{LC}$), as a function of energy. Because the densities are not well-determined, each time has two separate model runs, with the minimum density (5 cm^{-3}) determined from THEMIS-A ESA data, and the maximum density determined from EFI probe potentials. The strong diffusion limit is indicated by the black curve in panels c, d. This limit is exceeded for <100 keV electrons near 23 UT when THEMIS-A is near L=10, consistent with NOAA-18 results in Figure 3b, c.

To summarize, our low- and high-altitude comparative analysis, combined with model determination of the hiss-caused loss rate shows the following: solar wind pressure fluctuations modulate the magnetospheric cavity and produce fluctuations of large-scale magnetic and electric fields which drive a radial ExB drift. This drift modulates the populations of 10s keV electrons unstable to the growth of low frequency hiss, which then scatters <100 keV electrons into the atmosphere where they are subsequently observed as X-ray enhancements on BARREL.

5 Discussion and Conclusions

388 We have provided a comprehensive set of observations showing that solar wind pressure
389 structures, thought to originate at or near the Sun, drive large-scale modulations of electron loss
390 from the outer magnetosphere. Specifically, the pressure structures cause a forced breathing of
391 the magnetosphere which results in a radial ExB transport of plasma. This transport modulates
392 resonant electron populations that are unstable to the growth of low frequency hiss, which in turn
393 modulates electron loss from the outer magnetosphere. Prior to this study observations have
394 shown large-scale ULF-period modulation of: plasmaspheric hiss in association with electron
395 precipitation (Breneman et al., 2015), hiss and chorus (simultaneously) over large scales (J. Li et
396 al., 2017), chorus and electron cyclotron harmonic waves on the nightside flow-braking region
397 (Zhang et al., 2019), chorus and the pulsating aurora (Jaynes et al., 2015), kinetic Alfven waves
398 (Malaspina et al., 2015), EMIC waves in association with balloon duskside relativistic
399 precipitation events (Millan et al., 2013), to name a few. Taken together, these results suggest
400 that large-scale modulation of waves and precipitation occurs frequently, and at all local times
401 and in many different plasma regions.

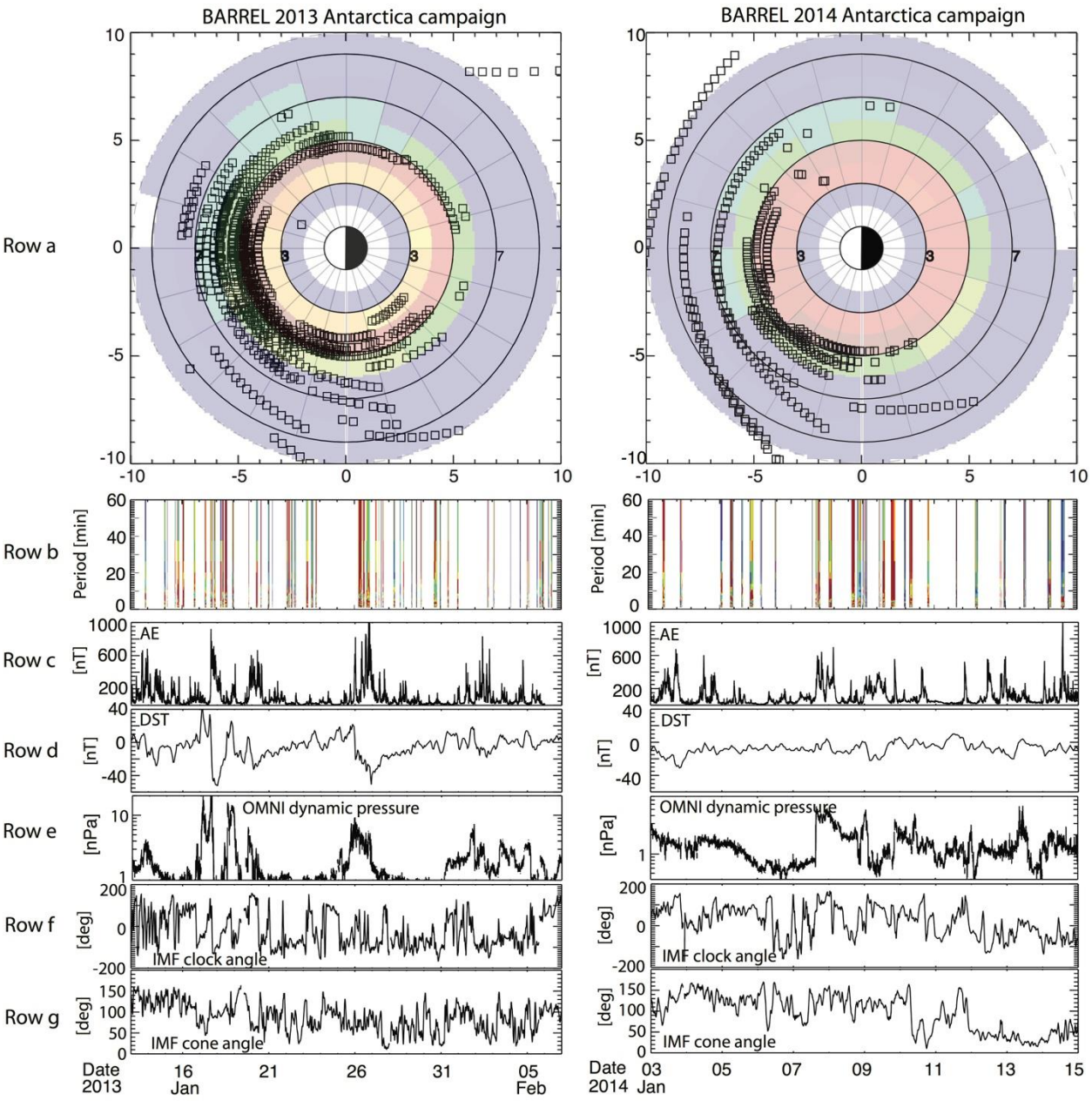

Figure 5: Location and time variation of coherence of 10-60 min periods of BARREL X-rays between spatially separated balloon pairs for the 2013 (left column) and 2014 (right column) Antarctica campaigns. Row a: L, MLT locations where coherence occurs for all possible balloon pairs. Each box shows the average position of a balloon pair for coherence of 10-60 min periods >0.7. For clarity, coherence values below 0.7 have been removed. The backdrop shows the overall sampling (adapted from Woodger et al., 2015). Row b: The frequency and time dependence of coherence of 10-60 min periods for each campaign. The color is the average coherence for all payload pairs observing coherence >0.7. Rows C-G show the relation of coherence to AE, DST, solar wind dynamic pressure, and the interplanetary magnetic field clock and cone angles (all from the OMNI database).

This idea is strongly supported by an analysis of the *coherence* of X-ray fluctuations for 10-60 min periods for spatially separated balloon pairs during the first two BARREL Antarctica campaigns (2013 and 2014). In each month-long campaign roughly 20 balloon payloads were launched, and at most times multiple balloons were simultaneously aloft. Figure 5 presents accumulated coherence results for both campaigns. Each box in row a marks the average position

of a balloon pair when significant coherence (>0.7) in X-rays at 10-60 minute periods is observed. The background color represents the overall balloon dwell time during each campaign. Coherence is observed almost exclusively on the dayside with peak MLT occurrence near noon or somewhat post-noon. It's unclear why there would be a post-noon tendency, but it may be related to the occasional existence of a plume, which has been noted by Degeling et al., 2018 to produce a post noon enhancement in ULF wave power. Peak L occurrence is at roughly L=4-5, likely influenced by the increased dwell time in this region. Because of the limited dataset, consisting of only a few dozen individual coherence *events* (defined as times when high coherence for any given balloon pair is observed continuously for two or more ~60 min periods) statistics are limited and no attempt has been made to calculate a likelihood of coherence for each L, MLT region. The maximum separation of any given balloon pair during times of high coherence is slightly period dependent and is in excess of 6 hrs MLT and 4 L for ~60 min periods. Shorter periods have smaller coherence scales on average and are less likely to be observed in general. This may in part be due to their scale size being shorter than the balloon separation.

Figure 5, row b plots the coherence for 10-60 min periods as a function of time for the most geomagnetically active portion of each campaign. Low coherence values have been removed for clarity. These plots clearly show the individual coherence events previously defined. Some coherence events have obvious drivers or triggers such as AE enhancements and DST fluctuations (rows c, d), solar wind pressure enhancements (row e), or magnetic field rotations (rows f, g). This is particularly true during the more dynamic 2013 campaign which included two minor storms and a number of moderate substorms. Many other events do not have an obvious driver. A majority of these non-driver events occur with a 24 hr cadence when the balloon pairs (largely fixed with respect to the Earth's surface) rotate to the noon MLT sector. This is most evident during the quiet 2014 campaign. This 24 hr repeatability suggests that dayside large-scale coherence of electron precipitation may often exist continually for days on end, but that balloons can only observe its X-ray signature when they are near noon MLT.

The preponderance of coherence events near noon local times, their large scale size, and frequent lack of obvious trigger internal to the magnetospheric (AE, DST), suggest that the driver of ~60 min coherence in electron precipitation is external to the magnetosphere. A preliminary analysis (not discussed here) shows that many of the coherence events in Figure 5 are likely initiated by changes in solar wind driving. Other processes such as magnetopause or magnetosheath waves (e.g. Wang et al., 2017; Archer et al., 2019), and foreshock structures (Russell and Hoppe, 2083; Takahashi et al., 2014) may also drive these large-scale dayside coherence events. Considering the ubiquity of solar wind mesoscale pressure structures of a few nPa or greater (Viall et al., 2009), coherence events may be a nearly continuous feature of the dayside outer radiation belt. Upcoming data from the Parker Solar Probe will help to decipher the cause of these structures.

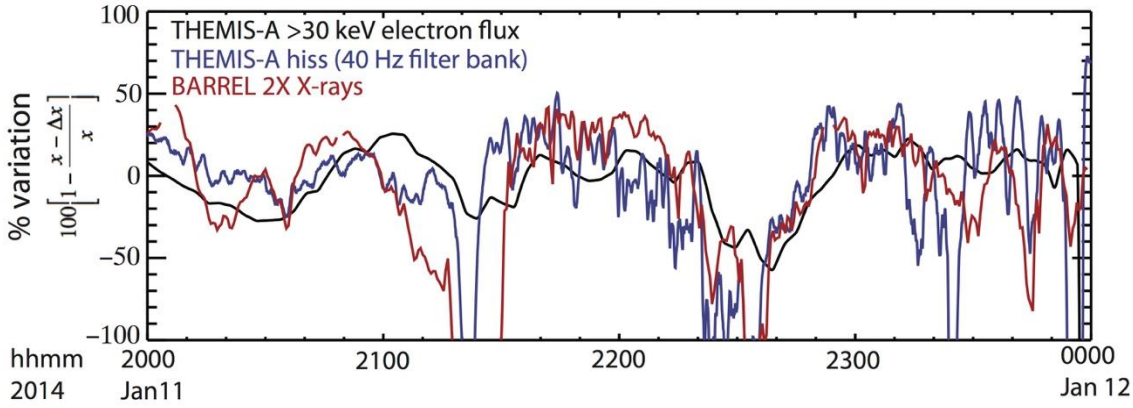

Figure 6: Percent variation of the following quantities relative to their 80 min smoothed version: THEMIS-A electron number flux (black), the low frequency plasmaspheric hiss amplitudes (blue, seen in the 40 Hz filter bank channel from Figure 2e), and 2X slow spectral (SSPC) X-rays integrated over >30 keV energies (red). The electron flux shows smooth variations while the hiss amplitude, and consequently X-rays, show behavior more consistent with a triggered emission.

These results suggest an important and fundamental link between low frequency (ULF to forced-breathing) wave power and wave scattering loss. As discussed by Zhang et al., 2019, even moderate changes in the resonance conditions brought about by forced breathing or ULF driving can push a system marginally stable to VLF wave growth into instability, causing a sudden increase in the precipitation loss that otherwise would not occur (Coroniti and Kennel, 1970). This thresholding is suggested for our conjunction event in Figure 6, which compares the percent change (over an 80 min smoothed background) for the THEMIS-A electron flux, hiss amplitudes, and BARREL 2X precipitation. The following can be noted. The hiss amplitudes drop to very low values until they appear to be suddenly triggered. Once triggered, they scale quite similarly with the THEMIS-A >30 keV electron flux on time scales of tens of minutes to an hour (though we note that they are much more bursty on few minute timescales). This suggests that modification of some parameter, modulated by the solar wind pressure, triggers the growth of hiss that otherwise would not exist, as is expected for a system driven to the threshold of instability. As discussed by Kennel and Petschek, 1966 the triggering of whistler mode wave growth requires a minimum pitch angle anisotropy and increases with the flux of resonant electrons. For this conjunction event (Figures 1, 2) the anisotropy observed by THEMIS-A essentially always exceeds the critical anisotropy, which is very low due to the low frequency of the hiss waves. These hiss waves are instead modulated by variations in the resonant electron flux, consistent in general with the results of Li et al., 2011 for larger L in the outer belt. This flux modulation can be due to the inward ExB motion of >30 keV electrons in the radially-outward phase space density gradient (Figure 3) and/or the expected few keV energization of ExB drifting electrons from conservation of their first adiabatic invariant.

The large spatial scale of these events and their high occurrence frequency suggests that it may be important to incorporate the effects of solar wind driving into models that predict atmospheric scattering loss due to plasmaspheric hiss. This may be particularly significant during periods of stronger driving (e.g. Kessel et al., 2008), which were not observed during the two BARREL campaigns. The importance of this externally driven hiss modulation may even extend to radiation belt energies (>100 keV) because hiss is known to provide important scattering loss of this population during storm recovery phase (e.g. Ripoll et al., 2013; Ni et al., 2014).

Acknowledgments

AWB and AJH acknowledge the NASA grant NNX15AF58G. WL, LC, and QM acknowledge the NSF grants AGS-1723588 and AGS-1847818, NASA grant NNX17AG07G, and the Alfred P. Sloan Research Fellowship FG-2018-10936. QM acknowledges the NASA support 80NSSC20K0196. JKS acknowledges NERC Grants NE/P017185/1 and NE/V002554/1. We'd like to thank Scott Boardsen for discussion of magnetosonic waves and Sam Califf for GOES satellite access. GOES-14 data can be accessed at https://satdat.ngdc.noaa.gov/sem/goes/data/science/mag/goes14_storage_mode_mag/. Satellite data for this paper were obtained using IDL SPEDAS software (http://themis.ssl.berkeley.edu/index.shtml) discussed in Angelopoulos et al., 2019. BARREL data are available at http://barreldata.ucsc.edu/data_products/. For OMNI data we acknowledge use of NASA/GSFC's Space Physics Data Facility's OMNIWeb (or CDAWeb or ftp) service at https://omniweb.gsfc.nasa.gov/. NOAA-18 (POES) data can be found at https://satdat.ngdc.noaa.gov/sem/poes/data/processed/ngdc/uncorrected/full/.

References

Agapitov, Oleksiy & Cheremnykh, Oleg. (2013). Magnetospheric ULF waves driven by external sources. Advances in Astronomy and Space Physics. 3. 12-19. Archer, M.O., Hietala, H., Hartinger, M.D. et al. Direct observations of a surface eigenmode of the dayside magnetopause. *Nat Comm* 10, 615 (2019). https://doi.org/10.1038/s41467-018-08134-5

Angelopoulos, V., Cruce, P., Drozdov, A. *et al.* The Space Physics Environment Data Analysis System (SPEDAS). *Space Sci Rev* 215, 9 (2019). https://doi.org/10.1007/s11214-018-0576-4

Boardsen, S. A., et al. (2016), Survey of the frequency dependent latitudinal distribution of the fast magnetosonic wave mode from Van Allen Probes Electric and Magnetic Field Instrument and Integrated Science waveform receiver plasma wave analysis, *J. Geophys. Res. Space Physics*, 121, doi:10.1002/2015JA021844.

Bonnell J.W. et al. (2009) The Electric Field Instrument (EFI) for THEMIS. In: Burch J.L., Angelopoulos V. (eds) The THEMIS Mission. Springer, New York, NY

Bortnik, Jacob & Thorne, Richard & Li, W. & Tao, Xin. (2016). Chorus Waves in Geospace and their Influence on Radiation Belt Dynamics: A Complex Interplay. 10.1093/acprof:oso/9780198705246.003.0009.

Breneman, A. et al., Global-scale coherence modulation of radiation-belt electron loss from plasmaspheric hiss, *Nature*, 2015.

Brito, T. V. et al., Ultralow frequency-wave induced losses, from *The Dynamic Loss of Earth's Radiation Belts, Elsevier*, 2020, Pages 29-48, https://doi.org/10.1016/B978-0-12-813371-2.00002-0.

Cattell, C. A., A. W. Breneman, S. A. Thaller, J. R. Wygant, C. A. Kletzing, and W. S. Kurth (2015), Van Allen Probes observations of unusually low frequency whistler mode waves observed in association with moderate magnetic storms: Statistical study, *Geophys. Res. Lett.*, 42, 7273–7281, doi:10.1002/2015GL065565.

Chaston, C. C., et al. (2014), Observations of kinetic scale field line resonances, *Geophys. Res. Lett.*, 41, 209–215, doi:10.1002/2013GL058507.

Chen, L., R. M. Thorne, J. Bortnik, and X.-J. Zhang (2016), Nonresonant interactions of electromagnetic ion cyclotron waves with relativistic electrons, *J. Geophys. Res. Space Physics*, *121*, 9913–9925, doi:10.1002/2016JA022813.

Coroniti, F. & Kennel, Charles. (1970). Electron precipitation pulsations. *Journal of Geophysical Research*. 75. 10.1029/JA075i007p01279.

Cully, C. M., J. W. Bonnell, and R. E. Ergun (2008), THEMIS observations of long-lived regions of large-amplitude whistler waves in the inner magnetosphere, *Geophys. Res. Lett.*, 35, L17S16, doi:10.1029/2008GL033643.

Degeling, A. W., Rae, I. J., Watt, C. E. J., Shi, Q. Q., Rankin, R., & Zong, Q.-G. (2018). Control of ULF wave accessibility to the inner magnetosphere by the convection of plasma density. *Journal of Geophysical Research: Space Physics*, *123*, 1086–1099. https://doi.org/10.1002/2017JA024874

Dungey, J. W. (1954a), Electrodynamics of the outer atmosphere, Pennsylvania State University Ionosphere Research Laboratory Science Report, 69.

Dungey, J. W. (1954b), The propagation of Alfvén waves through the ionosphere, Pennsylvania State University Ionosphere Research Laboratory Science Report, 57.

Dyrud, L. P., R. Behnke, E. L. Kepko, M. Sulzer, and S. Zafke (2008), Ionospheric ULF oscillations driven from above Arecibo, Geophys. Res. Lett., 35, L14101, doi:10.1029/2008GL034073.

Elkington, S. R., M. K. Hudson, and A. A. Chan, Resonant acceleration and diffusion of outer zone electrons in an asymmetric geomagnetic field, *J. Geophys. Res.*, 108(A3), 1116, doi:10.1029/2001JA009202, 2003.

Elkington, S. R. and Sarris, T. E., The Role of Pc-5 ULF Waves in the Radiation Belts: Current Understanding and Open Questions. *Waves, Particles, and Storms in Geospace*. First Edition. Georgios Balasis, Ioannis A. Daglis, Ian R. Mann. © Oxford University Press 2016. Published in 2016 by Oxford University Press.

568 Evans, D. S., and M. S. Greer (2004), Polar Orbiting Environmental Satellite Space Environment
569 Monitor-2: Instrument descriptions and archive data documentation, NOAA Tech. Mem. 93,
570 version 1.4, Space Weather Predict. Cent., Boulder, Colo.

571 Fenrich, F. R., and C. L. Waters (2008), Phase coherence analysis of a field line resonance and
572 solar wind oscillation, Geophys. Res. Lett., 35, L20102, doi:10.1029/2008GL035430.

573 Foat, J.E., et al., 1998. First detection of a terrestrial MeV X-ray burst. *Geophys. Res. Lett*.
574 Available from: https://doi.org/10.1029/1998GL900134.

575 Fu, S., Ni, B., Zhou, R., Cao, X., & Gu, X. (2019). Combined scattering of radiation belt
576 electrons caused by Landau and bounce resonant interactions with magnetosonic waves.
577 *Geophysical Research Letters*, 46. https://doi.org/10.1029/2019GL084438

578 Glassmeier, K.-H., et al. (2008), Magnetospheric quasi-static response to the dynamic
579 magnetosheath: A THEMIS case study, *Geophys. Res. Lett*., 35, L17S01,
580 doi:10.1029/2008GL033469.

581 Halford, A. J., et al. (2015), BARREL observations of an ICME-shock impact with the
582 magnetosphere and the resultant radiation belt electron loss, *J. Geophys. Res. Space Physics*,
583 *120*, 2557–2570, doi:10.1002/2014JA020873.

584 Hartinger, M. D., V. Angelopoulos, M. B. Moldwin, K. Takahashi, and L. B. N. Clausen (2013),
585 Statistical study of global modes outside the plasmasphere, *J. Geophys. Res. Space Physics*, 118,
586 804–822, doi:10.1002/jgra.50140.

587 Jaynes, A. N., et al. (2015), Correlated Pc4–5 ULF waves, whistler-mode chorus and pulsating
588 aurora observed by the Van Allen Probes and ground-based systems, *J. Geophys. Res. Space*
589 *Physics*, *120*, 8749–8761, doi:10.1002/2015JA021380.

590 Kennel, C. F., and Petschek, H. E. (1966), Limit on stably trapped particle fluxes, *J. Geophys.*
591 *Res.*, 71(1), 1– 28, doi:10.1029/JZ071i001p00001.

592 Kepko, L., Spence, H. E., and Singer, H. J., ULF waves in the solar wind as direct drivers of
593 magnetospheric pulsations, *Geophys. Res. Lett.*, 29(8), doi:10.1029/2001GL014405, 2002.

594 Kepko, L., and H. E. Spence (2003), Observations of discrete, global magnetospheric oscillations
595 directly driven by solar wind density variations, *J. Geophys. Res.*, 108(A6), 1257,
596 doi:10.1029/2002JA009676.

597 Kepko, L., N. M. Viall, S. K. Antiochos, S. T. Lepri, J. C. Kasper, and M. Weberg (2016),
598 Implications of L1 observations for slow solar wind formation by solar reconnection, *Geophys.*
599 *Res. Lett.*, *43*, 4089–4097, doi:10.1002/2016GL068607.

600 Kepko, L., & Viall, N. M. (2019). The source, significance, and magnetospheric impact of
601 periodic density structures within stream interaction regions. *J. Geophys. Res.: Space Physics*,
602 *124*, 7722–7743. https://doi.org/10.1029/ 2019JA026962

603 Kepko, L., Viall, N. M., & Wolfinger, K. (2020). Inherent length scales of periodic mesoscale
604 density structures in the solar wind over two solar cycles. *Journal of Geophysical Research:*
605 *Space Physics*, *125*, e2020JA028037. https:// doi.org/10.1029/2020JA028037 .

606 Kessel, R. L. (2008), Solar wind excitation of Pc5 fluctuations in the magnetosphere and on the
607 ground, *J. Geophys. Res.*, 113, A04202, doi:10.1029/2007JA012255.

608 Li, J., et al. (2017), Coherently modulated whistler mode waves simultaneously observed over
609 unexpectedly large spa- tial scales, J. Geophys. Res. Space Physics, 122, 1871‐1882,
610 doi:10.1002/ 2016JA023706.

611 Li, W., R. M. Thorne, J. Bortnik, Y. Nishimura, and V. Angelopoulos (2011), Modulation of
612 whistler mode chorus waves: 1. Role of compressional Pc4–5 pulsations, *J. Geophys. Res.*, 116,
613 A06205, doi:10.1029/2010JA016312.

614 Li, W., et al. (2013), An unusual enhancement of low-frequency plasmaspheric hiss in the outer
615 plasmasphere associated with substorm-injected electrons, *Geophys. Res. Lett.*, *40*, 3798–3803,
616 doi:10.1002/grl.50787.

617 Li, W., Q. Ma, R. M. Thorne, J. Bortnik, C. A. Kletzing, W. S. Kurth, G. B. Hospodarsky, and
618 Y. Nishimura (2015), Statistical properties of plasmaspheric hiss derived from Van Allen Probes
619 data and their effects on radiation belt electron dynamics, *J. Geophys. Res. Space Physics*, *120*,
620 3393–3405, doi:10.1002/2015JA021048.

621 Li, W., Shen, X.-C., Ma, Q., Capannolo, L., Shi, R., Redmon, R. J., et al. (2019). Quantification
622 of energetic Electron precipitation driven by plume whistler mode waves, Plasmaspheric hiss,
623 and exohiss. *Geophys. Res. Lett.*, 46, 3615– 3624. https://doi.org/10.1029/2019GL082095

624 Ma, Q., Li, W., Thorne, R. M., and Angelopoulos, V. (2013), Global distribution of equatorial
625 magnetosonic waves observed by THEMIS, *Geophys. Res. Lett*., 40, 1895- 1901,
626 doi:10.1002/grl.50434.

627 Ma, Q., Li, W., Thorne, R. M., Bortnik, J., Kletzing, C. A., Kurth, W. S., and Hospodarsky, G.
628 B. (2016), Electron scattering by magnetosonic waves in the inner magnetosphere, *J. Geophys.*
629 *Res. Space Physics*, 121, 274– 285, doi:10.1002/2015JA021992.

630 Malaspina, D. M., S. G. Claudepierre, K. Takahashi, A. N. Jaynes, S. R. Elkington, R. E. Ergun,
631 J. R. Wygant, G. D. Reeves, and C. A. Kletzing (2015), Kinetic Alfvén waves and particle
632 response associated with a shock-induced, global ULF perturbation of the terrestrial mag-
633 netosphere, *Geophys. Res. Lett.*, *42*, doi:10.1002/2015GL065935.

634 Malaspina, D. M., A. N. Jaynes, G. Hospodarsky, J. Bortnik, R. E. Ergun, and J. Wygant (2017),
635 Statistical properties of low-frequency plasmaspheric hiss, *J. Geophys. Res. Space Physics*, *122*,
636 doi:10.1002/2017JA024328.

637 Mann, I.R., Milling, D.K., Rae, I.J. *et al.* The Upgraded CARISMA Magnetometer Array in the
638 THEMIS Era. *Space Sci Rev* 141, 413–451 (2008). https://doi.org/10.1007/s11214-008-9457-6

639 Mann, I. R., et al. (2013), Discovery of the action of a geophysical synchrotron in the Earth's
640 Van Allen radiation belts, *Nat. Comm.*, 4, 2795, doi:10.1038/ncomms3795.

641 Mann, I., Ozeke, L., Murphy, K. *et al.* Explaining the dynamics of the ultra-relativistic third Van
642 Allen radiation belt. *Nature Phys* 12, 978–983 (2016). https://doi.org/10.1038/nphys3799

643 Mauk B.H., Fox N.J., Kanekal S.G., Kessel R.L., Sibeck D.G., Ukhorskiy A. (2012) Science
644 Objectives and Rationale for the Radiation Belt Storm Probes Mission. In: Fox N., Burch J.L.
645 (eds) The Van Allen Probes Mission. Springer, Boston, MA

646 McFadden J.P. et al. (2009) The THEMIS ESA Plasma Instrument and In-flight Calibration. In:
647 Burch J.L., Angelopoulos V. (eds) The THEMIS Mission. Springer, New York, NY

648 Menk, F., Kale, Z., Sciffer, M., Robinson, P., Waters, C., Grew, R., Clilverd, M., Mann, I.
649 (2014). Remote sensing the plasmasphere, plasmapause, plumes and other features using ground-
650 based magnetometers. *J. Space Weather and Space Climate*. 4. 10.1051/swsc/2014030.

651 Millan, R. M., and BARREL Team (2011), Understanding relativistic electron losses with
652 BARREL, *J. Atmos. Sol. Terr. Phys*., 73(11–12), 1425–1434.

653 Millan, R.M., McCarthy, M.P., Sample, J.G. *et al.* The Balloon Array for RBSP Relativistic
654 Electron Losses (BARREL). *Space Sci Rev* 179, 503–530 (2013).
655 https://doi.org/10.1007/s11214-013-9971-z

656 Mozer, F. S., Agapitov, O. V., Artemyev, A., Drake, J. F., Krasnoselskikh, V., Lejosne, S., and
657 Vasko, I. (2015), Time domain structures: What and where they are, what they do, and how they
658 are made. *Geophys. Res. Lett.*, 42, 3627– 3638. doi: 10.1002/2015GL063946.

659 Ni, B., et al. (2014), Resonant scattering of energetic electrons by unusual low- frequency hiss,
660 *Geophys. Res. Lett.*, 41, 1854–1861, doi:10.1002/2014GL059389.

661 Peck, E. D., C. E. Randall, J. C. Green, J. V. Rodriguez, and C. J. Rodger (2015), POES MEPED
662 differential flux retrievals and electron channel contamination correction, *J. Geophys. Res. Space*
663 *Physics*, 120, 4596–4612, doi:10.1002/2014JA020817.

664 Rae, I. J., Murphy, K. R., Watt, C. E. J., Halford, A. J., Mann, I. R., Ozeke, L. G., ... Singer, H. J.
665 (2018). The role of localized compressional ultra-low frequency waves in energetic electron
666 precipitation. *J. Geophys. Res,: Space Phys.*, 123, 1900–1914. https://
667 doi.org/10.1002/2017JA024674

668

669 Ripoll, J.-F., O. Santolík, G. D. Reeves, W. S. Kurth, M. H. Denton, V. Loridan, S. A. Thaller,
670 C. A. Kletzing, and D. L. Turner (2017), Effects of whistler mode hiss waves in March 2013, *J.*
671 *Geophys. Res. Space Physics*, 122, doi:10.1002/2017JA024139.

672 Roelof, E. C., and Sibeck, D. G. (1993), Magnetopause shape as a bivariate function of
673 interplanetary magnetic field *Bz* and solar wind dynamic pressure, *J. Geophys. Res.*, 98(A12),
674 21421– 21450, doi:10.1029/93JA02362.

675 Russell, C.T., Hoppe, M.M. Upstream waves and particles. *Space Sci Rev* 34, 155–172 (1983).
676 https://doi.org/10.1007/BF00194624
677
678 Sample, J. G., Millan, R. M., Woodger, L.A., Nanosat and balloon-based studies of radiation belt
679 loss: low-cost access to space, *The Dynamic Loss of Earth's Radiation Belts. From Loss in the*
680 *Magnetosphere to Particle Precipitation in the Atmosphere*, Elsevier, DOI:
681 https://doi.org/10.1016/B978-0-12-813371-2.00003-2, 2020.

682 Shi et al., (2020), Magnetosphere Response to Solar Wind Dynamic Pressure Change: Vortices,
683 ULF Waves, and Aurorae, *Dayside Magnetosphere Interactions, Geophysical Monograph 248*,
684 First Edition. Edited by Qiugang Zong, Philippe Escoubet, David Sibeck, Guan Le, and Hui
685 Zhang. © 2020 American Geophysical Union. Published 2020 by John Wiley & Sons, Inc.

686 Southwood, D. J., Some features of field line resonances in the magnetosphere, *Planet. Space*
687 *Sci*., 22, 483, 1974.

688 Spanswick, E. & Baker, G. (2005). Pc5 modulation of high energy electron precipitation: Particle
689 interaction regions and scattering efficiency. *Ann. Geophys.*. 23. 10.5194/angeo-23-1533-2005.

690 Stephenson, J.A.E. and Walker, A.D.M. (2002). HF radar observations of Pc5 ULF pulsations
691 driven by the solar wind. Geophys. Res. Lett., 29, 10.1029/2001GL014291.

692 Takahashi, K., Denton, R. E., Kurth, W., Kletzing, C., Wygant, J., Bonnell, J., Dai, L., Min, K.,
693 Smith, C. W., and MacDowall, R. (2015), Externally driven plasmaspheric ULF waves observed
694 by the Van Allen Probes, *J. Geophys. Res. Space Physics*, 120, 526– 552,
695 doi:10.1002/2014JA020373.

696 Turner, D., Shprits, Y., Hartinger, M. *et al.* Explaining sudden losses of outer radiation belt
697 electrons during geomagnetic storms. *Nature Phys* 8, 208–212 (2012).
698 https://doi.org/10.1038/nphys2185

699 Ukhorskiy, A. Y., B. J. Anderson, K. Takahashi, and N. A. Tsyganenko (2006), Impact of ULF
700 oscillations in solar wind dynamic pressure on the outer radiation belt electrons, *Geophys. Res.*
701 *Lett.*, 33, L06111, doi:10.1029/2005GL024380.

702 Viall, N. M., L. Kepko, and H. E. Spence (2008), Inherent length-scales of periodic solar wind
703 number density structures, *J. Geophys. Res*., 113, A07101, doi:10.1029/2007JA012881.

704 Viall, N. M., L. Kepko, and H. E. Spence (2009), Relative occurrence rates and connection of
705 discrete frequency oscillations in the solar wind density and dayside magnetosphere, *J. Geophys.*
706 *Res*., 114, A01201, doi:10.1029/2008JA013334.

707 Viall, N. M. and Vourlidas, A. (2015), Periodic density structures and the origin of the slow
708 solar wind, *The Astrophysical Journal*, Volume 807, Number 2

709 Villante, U., P. Francia, M. Vellante, P. Di Giuseppe, A. Nubile, and M. Piersanti (2007), Long-
710 period oscillations at discrete frequencies: A comparative analysis of ground, magnetospheric,
711 and interplanetary observations, J. Geophys. Res., 112, A04210, doi:10.1029/2006JA011896.

Villante, U., S. Di Matteo, and M. Piersanti (2016), On the transmission of waves at discrete frequencies from the solar wind to the magnetosphere and ground: A case study, J. Geophys. Res. Space Physics, 121, 380–396, doi:10.1002/ 2015JA021628.

Wang, C.-P., et al. (2017), A multispacecraft event study of Pc5 ultralow-frequency waves in the magnetosphere and their external drivers, *J. Geophys. Res. Space Physics*, 122, 5132–5147, doi:10.1002/ 2016JA023610.

Waters, C. L., F. W. Menk, and B. J. Fraser (1991), The resonance structure of low latitude Pc3 geomagnetic pulsations, *Geophys. Res. Lett., 18*, 2293–2296, doi:10.1029/91GL02550.

Woodger, L. A., A. J. Halford, R. M. Millan, M. P. McCarthy, D. M. Smith, G. S. Bowers, J. G. Sample, B. R. Anderson, and X. Liang (2015), A summary of the BARREL campaigns: Technique for studying electron precipitation, *J. Geophys. Res. Space Physics*, 120, 4922–4935, doi:10.1002/2014JA020874.

Xia, Z., Chen, L., Dai, L., Claudepierre, S. G., Chan, A. A., Soto-Chavez, A. R., & Reeves, G. D. (2016). Modulation of chorus intensity by ULF waves deep in the inner magnetosphere. *Geophys. Res. Lett.*, *43*, 9444–9452. https://doi.org/10.1002/2016GL070280

Zhang, X.-J., Chen, L., Artemyev, A. V., Angelopoulos, V., & Liu, X. (2019). Periodic excitation of chorus and ECH waves modulated by ultralow frequency compressions. *J. Geophys. Res.: Space Phys.*, *124*. https://doi.org/10.1029/ 2019JA027201

Zhou, X.-Z., Z.-H. Wang, Q.-G. Zong, R. Rankin, M. G. Kivelson, X.-R. Chen, J. B. Blake, J. R. Wygant, and C. A. Kletzing (2016), Charged particle behavior in the growth and damping stages of ultralow frequency waves: Theory and Van Allen Probes observations, *J. Geophys. Res. Space Physics*, *121*, 3254–3263, doi:10.1002/2016JA022447.

Zhu, X., and Kivelson, M. G. (1991), Compressional ULF waves in the outer magnetosphere: 1. Statistical study, *J. Geophys. Res.*, 96(A11), 19451– 19467, doi:10.1029/91JA01860.

Zhu, H., et al. (2015), Plasmatrough exohiss waves observed by Van Allen Probes: Evidence for leakage from plasmasphere and resonant scattering of radiation belt electrons, Geophys. Res. Lett., 42, 1012–1019, doi:10.1002/2014GL062964.

Figure 1.

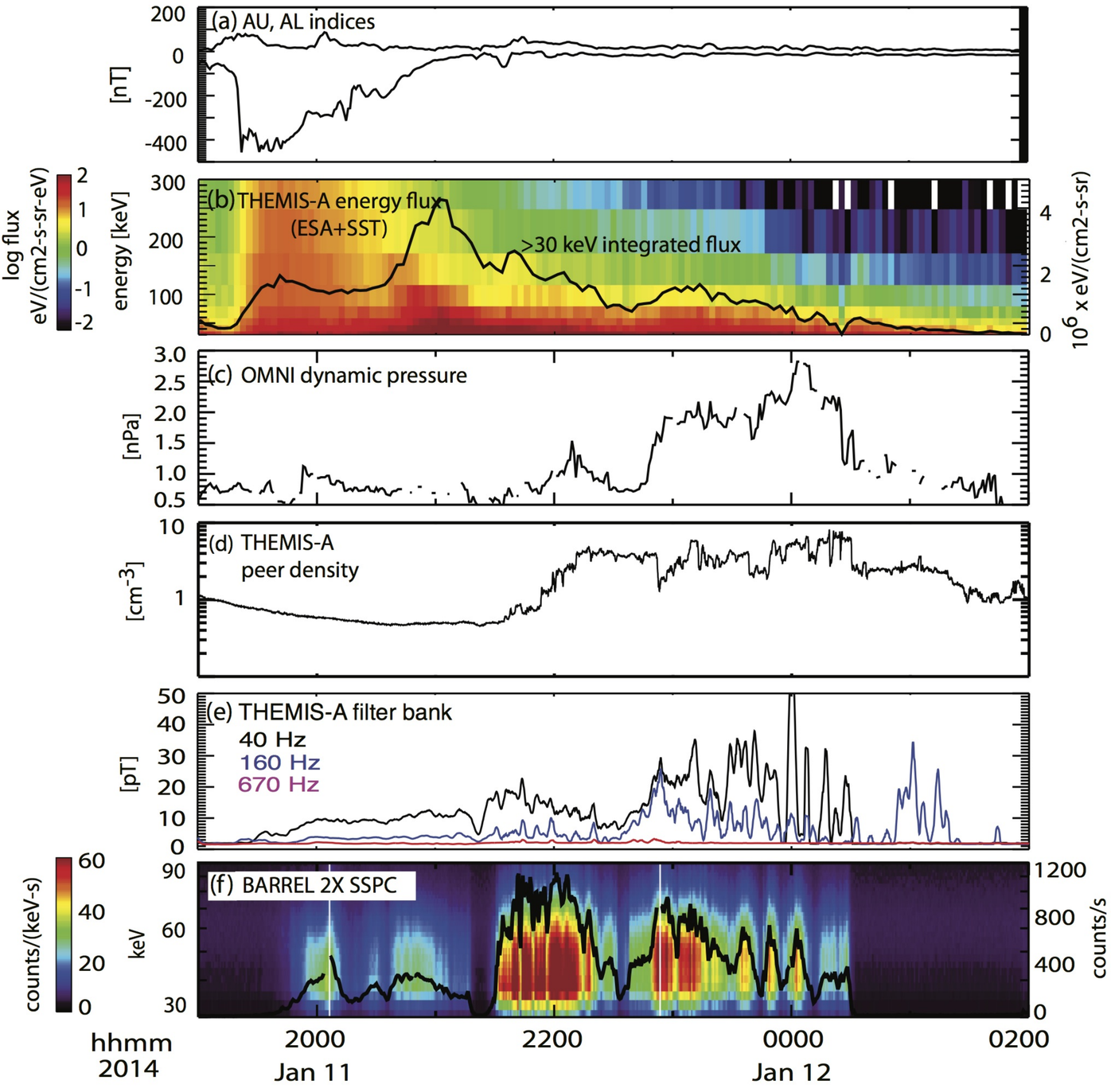
(a) AU, AL indices
[nT]
200
0
-200
-400
(b) THEMIS-A energy flux
(ESA+SST)
>30 keV integrated flux
energy [keV]
300
200
100
log flux
eV/(cm2-s-sr-eV)
2
1
0
-1
-2
10^6 x eV/(cm2-s-sr)
4
2
0
(c) OMNI dynamic pressure
[nPa]
3.0
2.5
2.0
1.5
1.0
0.5
(d) THEMIS-A
peer density
[cm^{-3}]
10
1
(e) THEMIS-A filter bank
40 Hz
160 Hz
670 Hz
[pT]
50
40
30
20
10
0
(f) BARREL 2X SSPC
keV
90
60
30
counts/(keV-s)
60
40
20
0
1200
800
400
0
counts/s
hhmm
2014
2000
Jan 11
2200
0000
Jan 12
0200
MLT
BARREL 2X 11.6 13.5 15.3 17.3
THEMIS-A 12.8 13.9 14.5 14.9
L
BARREL 2X 8.2 8.4 9.2 11.5
THEMIS-A 5.4 8.1 9.9 11.2
Altitude (km)
BARREL 2X 34.5 34.1 34.1 33.2

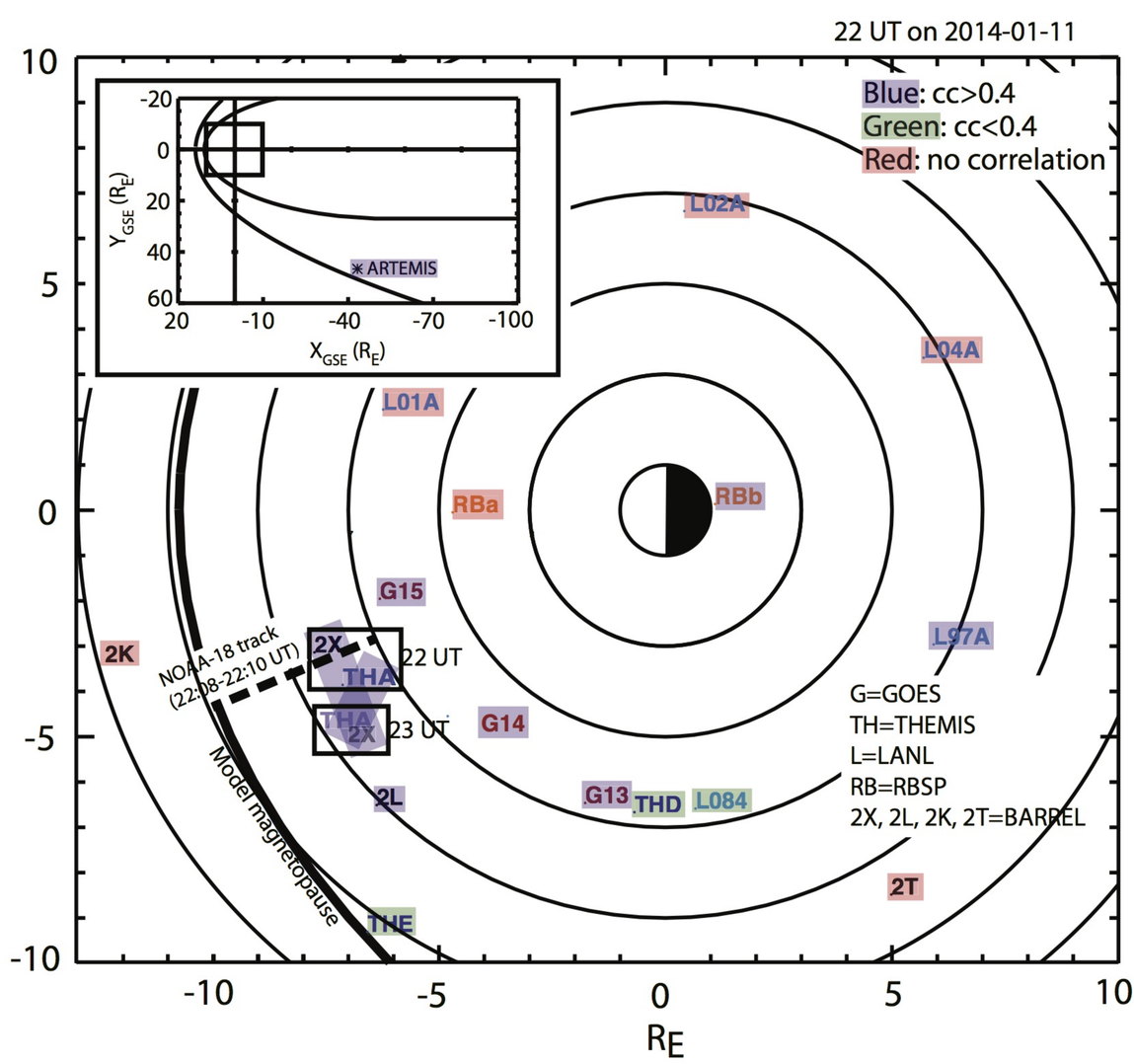
22 UT on 2014-01-11
Blue: cc>0.4
Green: cc<0.4
Red: no correlation
Y_{GSE} (R_E)
X_{GSE} (R_E)
ARTEMIS
L02A
L04A
L01A
RBa
RBb
G15
L97A
2K
NOAA-18 track
(22:08-22:10 UT)
2X
THA
22 UT
THA
2X
23 UT
G14
2L
G13
THD
L084
2T
THE
Model magnetopause
G=GOES
TH=THEMIS
L=LANL
RB=RBSP
2X, 2L, 2K, 2T=BARREL
R_E

Figure 2.

(a)
THEMIS-A |B| [nT]
OMNI HRO 1min Pressure [nPa]
(b)
THEMIS-A
Cumulative radial ExB transport + is Earthward [RE]
(c)
RBSP-A
(d)
THEMIS-A (ESA+SST) >30 keV flux [#/(s-cm2-sr)]
(e) Not detrended
THEMIS-A Filter bank SCM1 40 Hz channel [pT]
(f)
BARREL 2X SSPC >30 keV integrated [counts/sec]

hhmm 2014		2000 Jan 11	2100	2200	2300	0000 Jan 12
MLT	BARREL 2X	11.6	12.6	13.5	14.4	15.3
	THEMIS-A	12.8	13.5	13.9	14.2	14.5
L	BARREL 2X	8.2	8.2	8.4	8.7	9.2
	THEMIS-A	5.4	6.9	8.1	9.1	9.9
Altitude (km)	BARREL 2X	34.5	34.3	34.1	34.3	34.1

Figure 3.

(a)
21:45-22:05 UT
0-22° pitch angle bin
THEMIS-A
Electron flux
(e-/cm2-s-keV)
Energy (keV)
L=8
L=11
(b)
>30 keV
>100 keV
0° telescope
90° telescope
#/(cm2-s-sr)
POES NOAA-18
(c)
flux ratio (0°/90°)
>30 keV >100 keV
2014 Jan 11
hhmm 2207 2208 2209 2210 2211 2212
L (T89) 6.31 7.92 10.14 13.22 17.32 22.00
MLT 13.97 13.66 13.31 12.84 12.22 11.44

Figure 4.

22:00-22:05 UT

(a) Hiss spectrum

L = 8.2

B_o = 68.9 nT

B_w = 25.3 pT

B_w intensity [nT^2/Hz]

10^{-4} 10^{-5} 10^{-6} 10^{-7} 10^{-8} 10^{-9}

0.001 0.010 0.100 1.000

f/f_{ce}

22:58-23:03 UT

(b) Hiss spectrum

L = 9.1

B_o = 60.4 nT

B_w = 40.7 pT

B_w intensity [nT^2/Hz]

10^{-4} 10^{-5} 10^{-6} 10^{-7} 10^{-8} 10^{-9}

0.001 0.010 0.100 1.000

f/f_{ce}

(c)

D_{SD}

$\langle D_{\alpha\alpha} \rangle|_{LC}$

n_e=53 cm^{-3}

n_e=5 cm^{-3}

$D_{\alpha\alpha}$ (s^{-1})

10^{-2} 10^{-3} 10^{-4} 10^{-5} 10^{-6}

10^{-1} 10^{0} 10^{1} 10^{2} 10^{3}

E (keV)

(d)

D_{SD}

$\langle D_{\alpha\alpha} \rangle|_{LC}$

n_e=53 cm^{-3}

n_e=5 cm^{-3}

$D_{\alpha\alpha}$ (s^{-1})

10^{-2} 10^{-3} 10^{-4} 10^{-5} 10^{-6}

10^{-1} 10^{0} 10^{1} 10^{2} 10^{3}

E (keV)

Figure 5.

BARREL 2013 Antarctica campaign

BARREL 2014 Antarctica campaign

Row a

Row b

Row c

Row d

Row e

Row f

Row g

Period [min]

AE [nT]

DST [nT]

OMNI dynamic pressure [nPa]

IMF clock angle [deg]

IMF cone angle [deg]

Date 2013 16 Jan 21 26 31 05 Feb

Date 2014 Jan 03 05 07 09 11 13 15

Figure 6.

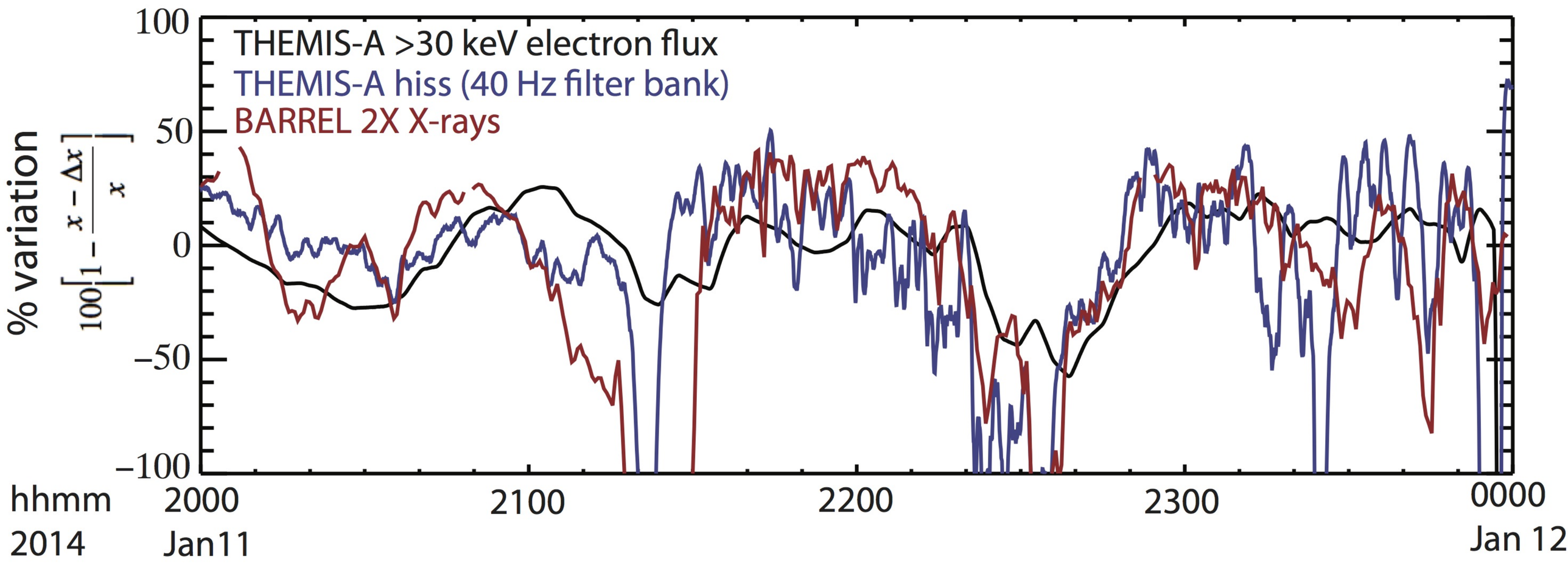
THEMIS-A >30 keV electron flux
THEMIS-A hiss (40 Hz filter bank)
BARREL 2X X-rays
% variation
$100\left[1-\frac{x-\Delta x}{x}\right]$
100
50
0
−50
−100
hhmm
2000
2100
2200
2300
0000
2014
Jan11
Jan 12